Title

Resolving tissue chromophore concentration at MRI resolution using multi-wavelength photo-magnetic imaging.

Journal

Biomedical Optics Express, 11(8)

ISSN

2156-7085

Authors

Algarawi, Maha
Erkol, Hakan
Luk, Alex
et al.

Publication Date

2020-08-01

DOI

10.1364/boe.397538

Peer reviewed

Research Article | Vol. 11, No. 8 / 1 August 2020 / Biomedical Optics Express 4244
Biomedical Optics EXPRESS

Resolving tissue chromophore concentration at MRI resolution using multi-wavelength photo-magnetic imaging

MAHA ALGARAWI,[1,2] HAKAN ERKOL,[3] ALEX LUK,[1] SEUNGHOON HA,[4] MEHMET B. ÜNLÜ,[3] GULTEKIN GULSEN,[1,2,5] AND FAROUK NOUIZI[1,5,*]

[1]Center for Functional Onco-Imaging, University of California Irvine, CA 92697, USA
[2]Department of Physics and Astronomy, University of California Irvine, CA 92697, USA
[3]Department of Physics, Bogazici University, Istanbul, Turkey
[4]Philips Healthcare, Pewaukee, WI 53002, USA
[5]Department of Radiological Sciences, University of California Irvine, CA 92697, USA
[*]fnouizi@uci.edu

Abstract: Photo-magnetic imaging (PMI) is an emerging optical imaging modality that showed great performance on providing absorption maps with high resolution and quantitative accuracy. As a multi-modality technology, PMI warms up the imaged object using a near infrared laser while temperature variation is measured using magnetic resonance imaging. By probing tissue at multiple wavelengths, concentration of the main tissue chromophores such as oxy- and deoxy-hemoglobin, lipid, and water are obtained then used to derive functional parameters such as total hemoglobin concentration and relative oxygen saturation. In this paper, we present a multi-wavelength PMI system that was custom-built to host five different laser wavelengths. After recovering the high-resolution absorption maps, a least-squared minimization process was used to resolve the different chromophore concentration. The performance of the system was experimentally tested on a phantom with two different dyes. Their concentrations were successfully assessed with high spatial resolution and average accuracy of nearly 80%.

1. Introduction

Employing non-ionizing near infrared (NIR) light (600-1000 nm) was established due to its ability to penetrate deep in biological tissue since such a medium exhibits a relatively low optical attenuation within this spectral range [1,2]. Based on this, NIR has been widely used in optical imaging to retrieve optical properties of biological tissue, which are directly related to the intrinsic chromophores responsible for the NIR light absorption such as oxy-hemoglobin, deoxy-hemoglobin, lipid, and water. It has been demonstrated that recovering the concentration of these chromophores provides essential insight on the angiogenesis or the hypermetabolism state of tumorous tissue, which correlates with its malignancy [3,4]. The contribution of each chromophore to the total absorption of the biological tissue at a given wavelength is linearly proportional to its attenuation coefficient [5]. Therefore, measurements at multiple wavelengths are necessary in order to differentiate between tissue chromophores and recover their absolute concentration [6–9].

Diffuse optical tomography (DOT) is one of the optical imaging modalities that provides functional information about the physiology of thick biological tissue. DOT is based on boundary measurements of diffused light traveling through tissue after its illumination using a NIR source of light [10–12]. These measurements are then used in a dedicated image reconstruction algorithm where the photon propagation is modelled and iteratively compared to the actual measurements to recover the optical absorption of tissue [13,14]. When performing multi-wavelength imaging, the

#397538 https://doi.org/10.1364/BOE.397538
Journal © 2020 Received 18 May 2020; revised 24 Jun 2020; accepted 30 Jun 2020; published 10 Jul 2020

Biomedical Optics EXPRESS

measurement acquired at each wavelength is processed individually to obtain the corresponding absorption at the applied wavelength. Afterwards, all the recovered wavelength dependent absorptions are used to obtain the different chromophores concentration using the Beer Lambert law [15]. DOT has become an important low-cost clinical research tool especially for breast cancer detection and characterization [16,17]. For example, it has been demonstrated that malignant tumors have higher total hemoglobin concentration and lower oxygen saturation level compared to normal tissue [18,19]. Yet, translation of DOT as a routine imaging modality has been largely delayed due to its poor spatial resolution [20]. Nevertheless, extensive efforts have been made to improve the performance of DOT. Its combination with anatomical imaging modalities has been widely demonstrated to improve its spatial resolution through the use of structural *a priori* information [21–24]. However, although this approach successfully improves the image spatial resolution, it usually fails when the functional information does not match the anatomical boundaries of internal organs or tumors [25].

Previously, Photo-Magnetic Imaging (PMI) has been introduced to overcome the limitations of the conventional multi-modality approach. PMI is a true multi-modality imaging technique that uses a novel approach to combine diffuse optics with magnetic resonance imaging (MRI). PMI utilizes a NIR laser to warm up the tissue while the internal induced temperature distribution is measured using Magnetic Resonance Thermometry (MRT) [26]. Unlike standard multi-modality approaches, PMI does not utilize MRI to provide structural *a priori* information, but to measure the internal laser-induced temperature [27–29]. The observed temperature rise is proportional to the tissue absorption coefficient as well as the amount of locally absorbed light. Consequently, high-resolution optical absorption maps can be recovered from the measured MRT temperature maps using a dedicated PMI image reconstruction algorithm [27,30]. During this image reconstruction process, the absorption map at a given wavelength is reconstructed by iteratively minimizing the difference between the measured and simulated temperature maps, which are obtained by solving the combined diffusion and Pennes' bio-heat thermal equations [27,30–32]. PMI provides absorption maps with high resolution and quantitative accuracy since the temperature measurements are acquired internally making its inverse problem well-posed. The superior performance of single wavelength PMI technique on recovering high-resolution absorption maps has been demonstrated with various simulation and experimental studies [27,29,33,34].

Recently, we built a new PMI system that hosts multiple high-power laser wavelengths allowing to perform multi-wavelength measurements and retrieve chromophore concentration with high-resolution and quantitative accuracy [35]. In this paper, we present preliminary experimental validation of our multi-wavelength PMI system. Multi-wavelength PMI was used to recover the concentration of two different NIR dyes imbedded in an agar phantom. The temperature maps were measured using MRT at three wavelengths. Next, PMI image reconstruction algorithm was used to recover the high-resolution absorption map at each wavelength. Finally, the three recovered absorption maps were then used to accurately obtain the concentration of the two dyes. For this step, a new algorithm was implemented to recover the concentration by a non-negative linear least square minimization. The high performance of multi-wavelength PMI on recovering chromophore concentration brings PMI a step closer to being a high-resolution preclinical diagnosing tool for *in vivo* imaging.

2. Materials and methods

2.1. Multi-wavelength PMI system

The experimental study is performed with our home-built PMI system which hosts five high-power continuous-wave lasers with wavelengths ranging between 760 nm and 980 nm. A cooling system was custom-built to monitor and control the laser operating temperature. The PMI system is fully automated and controlled via a versatile LabVIEW-based software in order to allow

Biomedical Optics EXPRESS

synchronization of the lasers operation and the MRT data acquisition. To facilitate the mobility of PMI system, the laser diodes, their drivers and the cooling system as well as a control computer are all assembled on a compact cart, as shown in Fig. 1(a).

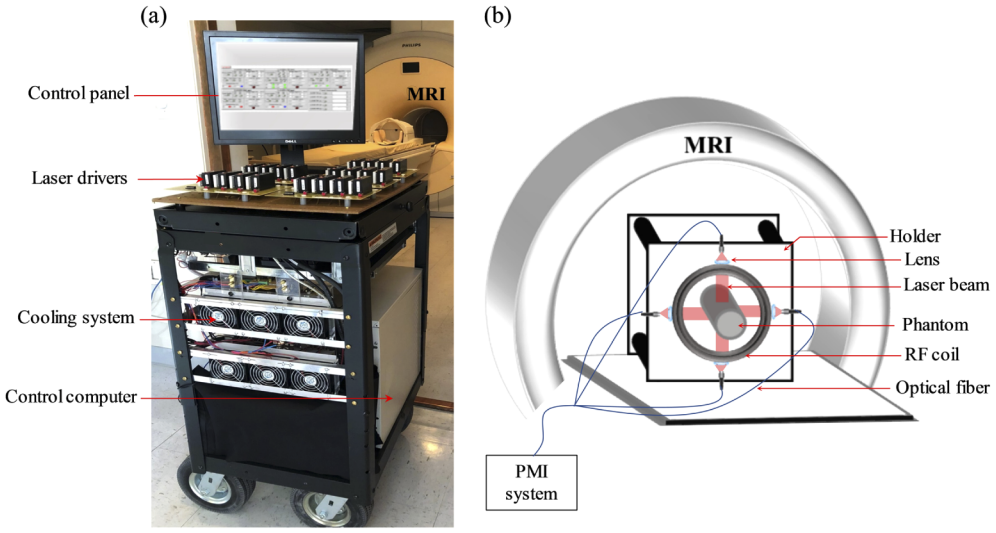

Fig. 1. (a) Photography of the multi-wavelength PMI system. (b) Schematic of the PMI interface showing the phantom inside the RF-coil with four illumination windows.

A 3 Tesla MRI system (Achieva, Philips) is used to monitor the internal spatiotemporal temperature distribution of the phantom by acquiring MRT measurements. A15 m long optical fiber is used to transfer laser light from the PMI system located in the MRI control room to the phantom, which is placed inside a small animal home-built RF-coil [28]. Before reaching the phantom, laser light is collimated using a collimation lens (35 mm, Newport Corporation) to provide uniform illumination at the phantom surface. Figure 1(b) shows a schematic of the PMI interface which consists of the RF-coil having four illumination windows and their collimation lens.

The MRT temperature maps are obtained using the proton resonance frequency (PRF) shift method with a gradient echo sequence using 60 ms and 12 ms as repetition and echo time, respectively. Technically, MRT requires the acquisition of at least two phase maps since the relative temperature change is linearly proportional to the measured phase variation [26]. Here, a dynamic MRT acquisition is initiated using three phase maps to be used as baseline, heating and cooling phase maps. Each of these phase maps is acquired during 6 seconds [27]. Finally, the relative temperature variation is obtained using the Larmor equation based on the phase difference between the three phases [28].

2.2. PMI Image reconstruction algorithm

Once the MRT temperature maps acquired, they are used in the PMI image reconstruction algorithm to obtain a high-resolution absorption map at each wavelength. During this process, the simulated time-dependent temperature map is generated by solving PMI forward problem using finite element method (FEM) [27,30]. In this forward problem, the photon propagation and heat transfer in the medium are modelled by solving the diffusion and the bio-heat equations, respectively.

$$\begin{cases} -\nabla[D(r)\nabla\Phi(r)] + \mu_a(r)\Phi(r) = S(r) \\ \rho c\frac{\partial T(r,t)}{\partial t} - \nabla[k\nabla T(r,t)] = \mu_a(r)\Phi(r) \end{cases} \quad (1)$$

Biomedical Optics EXPRESS

where $\Phi(r)$ [W.mm^{-2}] is the photon density at position r [mm], D [mm] is the diffusion coefficient, $D(r) = 1/(3(\mu_a + \mu_s'))$, μ_a [mm^{-1}] and μ_s' [mm^{-1}] are the absorption and reduced scattering coefficients, respectively. $S(r)$ [W.mm^{-3}] is the source of light, ρ (kg.m^{-3}) is the density, c [J.(kg.°C)$^{-1}$] is the specific heat, and k [W.(mm.°C)$^{-1}$] is the thermal conductivity of the medium. Note that, in this combined system of equation, the photon density resulting from the resolution of the diffusion equation is used to calculate the thermal energy source, which is defined as the product of the photon density and the local absorption coefficient μ_a.

These simulated temperature maps are then used during the PMI inverse problem, for each wavelength individually. Here, the optical absorption maps are obtained by minimizing an objective function of the quadratic error between the simulated and the measured MRT temperature maps [27,30]:

$$\Omega(\mu_a) = \arg\min_{\mu_a} \sum_{n=1}^{N} ||T_n^m - T_n(\mu_a)||^2 \tag{2}$$

where T^m and T are the measured MRT and the simulated temperature maps, respectively. N is the FEM mesh number of nodes. Using PMI inverse problem, the unknown μ_a at each wavelength is iteratively updated using the Levenberg–Marquardt minimization method by [36]:

$$\Delta\mu_a = (J^T J + \gamma I)^{-1} J^T (T^m - T(\mu_a)) \tag{3}$$

where J is the Jacobian matrix, γ is a regularization parameter, and I is the identity matrix.

Finally, the chromophore concentration is recovered at each node of the FEM mesh using the following equation [15]:

$$\mu_{a_{tot}}(\lambda) = \sum_{m=1}^{M} \mu_{a_m} = ln10 \sum_{m=1}^{M} \varepsilon_m(\lambda) C_m \tag{4}$$

where $\mu_{a_{tot}}$ [Λx1] is the total recovered absorptions with Λ being the number of applied wavelengths. λ is the used laser wavelength. M is the number of considered chromophores in the object, ε [Λx M] is the wavelength-dependent extinction coefficient, and C [Mx1] is the unknown chromophore concentration.

2.3. Experimental settings

Here, we present preliminary results obtained using our multi-wavelength PMI system. This experimental study was performed to evaluate the performance of multi-wavelength PMI in recovering chromophore concentration within a mice-sized phantom. The used phantom consists in a 25 mm diameter cylindrical agar phantom with two embedded 4 mm diameter inclusions, Fig. 2(a). The absorption coefficient of these inclusions is set to be higher than the background to simulate a cancerous tumor [37]. Inclusion 1 and Inclusion 2 are respectively positioned 5.2 mm and 7.3 mm deep under the upper surface of the phantom, Fig. 2(a).

The absorption coefficient of the phantom's background is set using a black ink-based dye having a quasi-flat absorption spectrum in the NIR spectral region. The concentration of this dye is adjusted to provide an absorption coefficient of 0.009 mm^{-1}. Two NIR dyes (Dye 1: NIR869A and Dye 2: NIR782E, QCR solutions Corp, USA) were used in Inclusion 1 and Inclusion 2, respectively. Each of these two dyes has a different absorption spectrum in the NIR spectral region with a peak absorption at 869 nm for Dye 1, and at 782 nm for Dye 2, Fig. 2(b). The concentration [C] of both dyes were set to $C_{Dye1} = 0.014$ M and $C_{Dye2} = 0.009$ M to obtain an absorption contrast with respect to the phantom's background. In this study, the phantom is only illuminated from its top side as represented with the red arrow in Fig. 2(a). Three illumination wavelengths were used (780 nm, 808 nm, and 860 nm). These wavelengths were chosen for this study since two of them are matching with the absorption peak of these two dyes, while the 808 nm laser is close to the isosbestic point. The absorption coefficients at each wavelength of these two inclusions as well as the background are summarized in Table 1.

Biomedical Optics EXPRESS

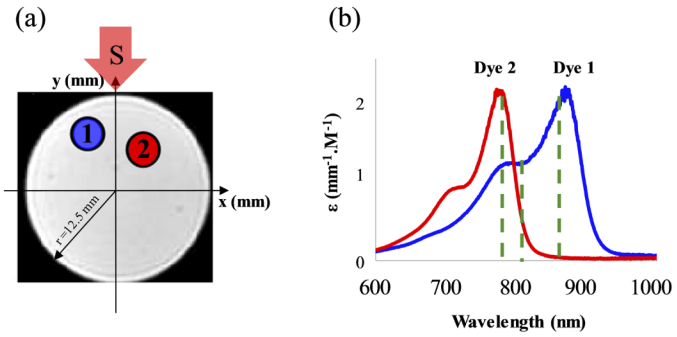

Fig. 2. (a) Axial T1-weighted MR image showing a cross-section of the 25 mm diameter cylindrical phantom. The inclusions are sketched on the phantom to show their size and position. (b) Extinction coefficient spectra of the two used dyes. The spectrum of Dye 1, used to fill Inclusion 1, is highlighted in blue, while the spectrum of Dye 2, used in Inclusion 2, is presented in red.

Table 1. The real absorption coefficient of Inclusion 1 and Inclusion 2 at the three used wavelengths (mm^{-1}).

	780 nm	808 nm	860 nm
Inclusion 1	0.023	0.023	0.038
Inclusion 2	0.026	0.014	0.0094
Background	0.009	0.009	0.009

3. Results

3.1. Multi-wavelength MRT temperature measurements

Multi-wavelength temperature measurements were collected to recover the concentration of the dye in each inclusion. The laser-induced temperature was measured using MRT at each wavelength sequentially. For each wavelength, the phantom was heated for 6 seconds, while respecting the maximum permissible exposure limits for skin as defined by the American National Standards Institute. After each measurement, a break of two minutes was respected to allow the phantom to return to its baseline temperature. The MRT temperature maps at the three wavelengths are shown in Fig. 3.

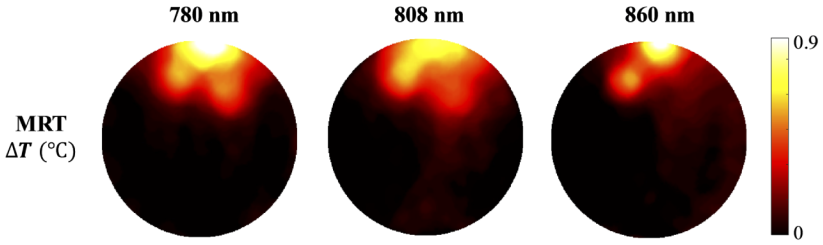

Fig. 3. The temperature maps measured experimentally using MRT at 780 nm, 808 nm and 860 nm. The phantom was only heated for 6 seconds.

As previously mentioned, the phantom was only illuminated from its top surface. Consequently, all temperature maps show a high increase in temperature under the illumination site. The increase in temperature at each wavelength depends on the position of the inclusion (distance from the source) as well as its local absorption coefficient, Fig. 2(a). This is clearly noticed

Biomedical Optics EXPRESS

in the temperature maps acquired at 808 nm and 860 nm, where Inclusion 1 shows a higher increase in temperature compared to Inclusion 2. This is because Inclusion 1 was positioned closer to the source and it has a higher absorption coefficient at these two wavelengths. However, a comparable increase in temperature is observed in both inclusions at 780 nm.

For further comparison, the real absorption coefficients of the dyes, summarized in Table 1, were used to generate simulated temperature maps using the PMI forward problem, Eq. (1). Figure 4 shows that these simulated temperature maps exhibit similar behavior as the one observed on the MRT measured maps, Fig. 3.

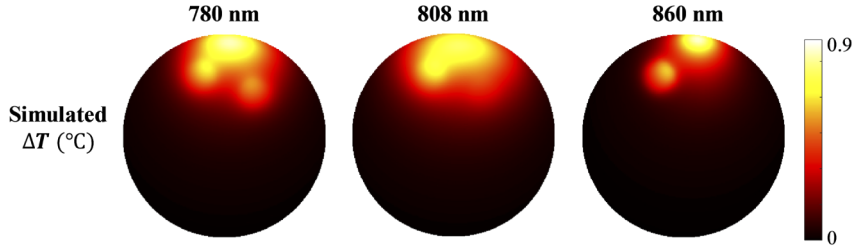

Fig. 4. The simulated temperature maps at 780 nm, 808 nm and 860 nm. The phantom was only heated for 6 seconds.

3.2. *Multi-wavelength absorption coefficient reconstruction*

For each wavelength, the measured temperature map was used as an input for the PMI inverse problem to recover the high-resolution and quantitatively accurate corresponding absorption map using Eq. (3), Fig. 5.

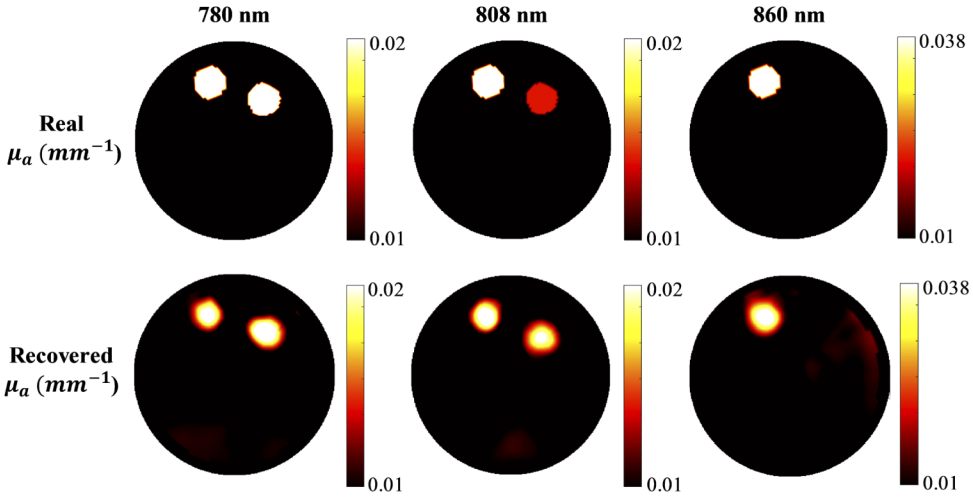

Fig. 5. The real absorption maps (top) and the recovered absorption maps at 780 nm, 808 nm, and 860 nm (bottom).

As expected, the reconstructed absorption maps follow the dyes spectra presented in Fig. 2(b). Also, these absorption maps show that both inclusions are recovered with high-resolution regardless of their depth or position within the phantom. The accuracy of the recovered absorption map at each wavelength demonstrate the high performance of PMI. Indeed, the average error of the recovered absorption coefficient at the three wavelengths is as low as 14%

Biomedical Optics EXPRESS

for Inclusion 1 and 21% for Inclusion 2. This error represents the average mean absolute percentage error calculated at each wavelength, for each inclusion. However, one can observe some reconstruction artifacts resulting from the minimization process using Eq. (3). Nevertheless, these artifacts are minimal since they only represent approximately 15% of the local absorption of the dyes. Please note that these absorption maps are obtained after only heating the phantom for 6 seconds. This heating period allows to increase the internal temperature of the phantom to only 0.9 °C, which is approximately nine times higher than the MRT noise level of 0.1 °C [27,29]. We previously demonstrated the ability of PMI to overcome this limitation by increasing the number of illumination windows from one to four illumination windows to increase the signal to noise ratio, which consequently increases heating depth penetration [27]. In addition, Lin *et. al.* demonstrated that using longer heating times allows to better warm up the medium, but in detriment of the overall imaging time [30]. Table 2 summarizes the mean and standard deviation of the recovered absorption coefficient values.

Table 2. Mean and standard deviation of the recovered absorption coefficient (mm^{-1}) of Inclusion 1 and Inclusion 2 at the three used wavelengths.

	780 nm	808 nm	860 nm
Inclusion 1	0.0182 ± 0.0019	0.0193 ± 0.0019	0.0365 ± 0.0031
Inclusion 2	0.0205 ± 0.0020	0.0179 ± 0.0015	0.0108 ± 0.0002
Background	0.0093 ± 0.0006	0.0092 ± 0.0005	0.0095 ± 0.0010

3.3. Chromophore concentration recovery

After solving the PMI inverse problem, the recovered absorption maps were then used in Eq. (4) to resolve the concentration maps of the two dyes. Figure 6 depicts the calculated concentration maps of the two dyes. Due to the high resolution and accuracy of the recovered absorption maps, these concentration maps were recovered accurately with an average error of 13% and 25% for Dye 1 and Dye 2, respectively. As expected, one can observe some artifacts in the concentration maps resulting from the minimization process using Eq. (4). These artifacts resulted from the ones previously observed in the absorption maps. Nevertheless, these artifacts are minimal since they only represent an average of 13% of the concentration of the dyes.

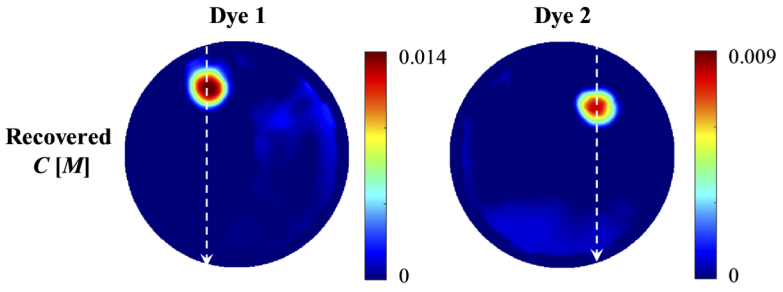

Fig. 6. The recovered molar concentration maps of Dye 1 (left) and Dye 2 (right) obtained using the absorption maps in Fig. 5 and Eq. (4). The dashed lines show the position of the profiles presented in Fig. 7.

To further quantify the performance of multi-wavelength PMI in resolving chromophores concentration in a turbid medium, profiles along the y-axis passing through the center of each inclusion are performed as shown in Fig. 7.

Biomedical Optics EXPRESS

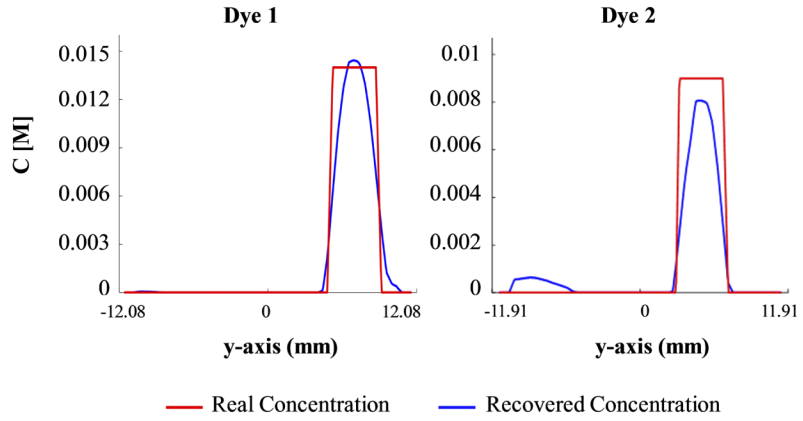

Fig. 7. The profiles carried along the y-axis of the dye concentration map at the center of each inclusion: the real concentration (red line) and the recovered concentration (blue line).

These profiles prove the PMI robustness on recovering chromophore concentration in a tissue-like phantom. Please note that these high-resolution and quantitative accuracy maps are obtained without the use of any *a priori* information from the anatomical MRI images.

4. Discussion

DOT has shown a great potential in monitoring blood volume and oxygen saturation levels in biological tissue; however, its translation to the clinical arena is still hampered due to its low spatial resolution and quantitative accuracy. Incorporating DOT with anatomical imaging modality such as MRI [38], X-ray [39], or ultrasound [17,40] has significantly improved the quality of DOT reconstructed images. In this approach, DOT image reconstruction algorithm uses the structural information provided by the anatomical imaging modality as *a priori* information [24]. In fact, this approach not only enhances the image spatial resolution of DOT but also improves its quantitative accuracy. However, the drawback of this approach occurs when the structural boundaries provided by the anatomical imaging modality do not correlate with the functional information recovered by DOT [41].

PMI has been introduced to overcome these limitations. It utilizes lasers to induce a relatively low temperature increase in biotissue, while monitoring it using MRT. Therefore, PMI is considered a true multimodality technique since it utilizes both modalities synergically, unlike conventional multimodality techniques. PMI has demonstrated a high performance on providing chromophore concentration maps with high resolution and quantitative accuracy. However, in its current form, the PMI technique is limited to only recovering the absorption coefficient of the tissue. Consequently, the scattering coefficient is considered known and is attributed to the entire volume, when performing phantom studies. In real applications, always prescribed T1-weighted MR images can be used to define different organs/regions and individual scattering coefficient values can be assigned based on available literature.

MRT is the pivotal component of PMI in providing high resolution images. In fact, in addition to performing internal measurements within tissue, MRT measurements have a unique feature of being completely depth independent. In fact, MRT temperature maps are solely obtained from variations of the proton resonance frequency phase maps. These phase maps are accurately measured everywhere within the imaged medium and are totally independent from depth or the distance from the used laser. The measured MRT phase maps have a characteristic noise with a gaussian distribution between -0.05 C° and +0.05 C° [42]. Since temperature maps are

Biomedical Optics EXPRESS

proportional to the difference in phase maps, noise level of MRT temperature maps is defined as twice the phase standard deviation and is equal to 0.1 C° everywhere within the MRT image.

On the other hand, the depth limitation of PMI depends on its ability to warm up deep regions above the MRT noise level. Previously, we demonstrated that this issue can be overcame by simultaneously using all four illumination spots allowed by our custom-designed RF-coil, Fig. 1(b) [27]. Further, in order to test the feasibility of PMI for breast imaging, a simulation study was conducted to investigate the possibility of warming up the center of a breast-like phantom. Results showed that the temperature at the center of the phantom can be indeed increased above the noise level using the four ports illumination configuration. Since the dynamic range of temperature difference measurements is very limited over the whole imaging volume, 0.1 C° noise level is enough to probe more than one inch under any illumination port depending on the tissue type and its overall absorption.

Being a low-cost and non-contact add-on to MRI, PMI can provide critical additional functional information; hence, it has enormous potential to assist MRI in the detection, diagnosis, and therapy monitoring of various diseases.

5. Conclusion

PMI has been introduced as a functional imaging technique that provides optical absorption maps with high resolution and quantitative accuracy. In order to leverage the valuable information provided by PMI, the obtained absorption maps need to be translated into chromophores concentration maps, which are directly related to the physiology of the bio-tissue. Moreover, this would allow PMI to provide the distribution of exogenous contrast agents such as ICG and gold nanoparticles which are useful to detect and characterize tumors [43,44]. Therefore, we upgraded our PMI technique from utilizing single wavelength to multiple wavelengths and built a system designed to host five laser wavelengths (760, 780, 808, 860, and 980 nm). In this study, the performance of the multi-wavelength PMI was demonstrated on a phantom with two embedded inclusions, each inclusion filled with NIR dye. Based on the absorption spectra of the dyes, three wavelengths were chosen to be used in this experiment. The laser-induced temperature was measured using MRT at each wavelength. Then, each temperature map was used in the image reconstruction algorithm to recover the corresponding absorption map at the employed wavelength. Finally, the concentration of each dye was recovered successfully from the recovered absorption maps using the Beer Lambert law.

For future *in vivo* studies, employing more wavelengths will allow to recover more endogenous chromophores such as lipid and water alongside oxy- and deoxy-hemoglobin. These chromophores concentrations are demonstrated to be directly correlated with the malignancy of tumorous tissue [45]. Finally, our technique demonstrated its high performance to be used as a safe and accurate diagnosis tool for tumor detection and characterization.

Funding

Susan G. Komen (KG101442); TUBITAK (2009K120520); Bogazici University (BAP 15362); Imam Mohammed Ibn Saud Islamic University; Ruth L Kirschstein National Research Service Award (F31CA171915-01A1); Fulbright Association; National Institutes of Health (P30CA062203, R01EB008716, R21CA170955, R33CA120175).

Disclosures

The authors declare no conflicts of interest.

Biomedical Optics EXPRESS

References

1. S. K. V. Sekar, A. Dalla Mora, I. Bargigia, E. Martinenghi, C. Lindner, P. Farzam, M. Pagliazzi, T. Durduran, P. Taroni, and A. Pifferi, "Broadband (600–1350 nm) time-resolved diffuse optical spectrometer for clinical use," IEEE J. Sel. Top. Quantum Electron. **22**(3), 406–414 (2016).
2. S. L. Jacques, "Optical properties of biological tissues: a review," Phys. Med. Biol. **58**(11), R37–R61 (2013).
3. H. S. Yazdi, T. D. O'Sullivan, A. Leproux, B. Hill, A. Durkin, S. Telep, J. Lam, S. S. Yazdi, A. M. Police, and R. M. Carroll, "Mapping breast cancer blood flow index, composition, and metabolism in a human subject using combined diffuse optical spectroscopic imaging and diffuse correlation spectroscopy," J. Biomed. Opt. **22**(4), 045003 (2017).
4. M. G. Pakalniskis, W. A. Wells, M. C. Schwab, H. M. Froehlich, S. Jiang, Z. Li, T. D. Tosteson, S. P. Poplack, P. A. Kaufman, B. W. Pogue, and K. D. Paulsen, "Tumor angiogenesis change estimated by using diffuse optical spectroscopic tomography: demonstrated correlation in women undergoing neoadjuvant chemotherapy for invasive breast cancer?" Radiology **259**(2), 365–374 (2011).
5. W. Cong, X. Intes, and G. Wang, "Optical tomographic imaging for breast cancer detection," J. Biomed. Opt. **22**(09), 1 (2017).
6. M. Algarawi, A. Luk, H. Erkol, M. Almudhry, B. M. Unlu, G. Gulsen, and F. Nouizi, "Reconstruction chromophore concentration directly by Photo-Magnetic Imaging: simulation study," in *Clinical and Translational Biophotonics*, (Optical Society of America, 2020), JTu3A. 15.
7. M. Algarawi, F. Nouizi, A. Luk, M. Mehrabi, H. Erkol, M. B. Ünlü, G. Gulsen, and S. Ha, "High-resolution chromophore concentration recovery using multi-wavelength photo-magnetic imaging," Proc. SPIE **10871**, 108710F (2019).
8. S. Vasudevan, F. Forghani, C. Campbell, S. Bedford, and T. D. O'Sullivan, "Method for Quantitative Broadband Diffuse Optical Spectroscopy of Tumor-Like Inclusions," Appl. Sci. **10**(4), 1419 (2020).
9. D. Lighter, J. Hughes, I. Styles, A. Filer, and H. Dehghani, "Multispectral, non-contact diffuse optical tomography of healthy human finger joints," Biomed. Opt. Express **9**(4), 1445–1460 (2018).
10. A. T. Eggebrecht, S. L. Ferradal, A. Robichaux-Viehoever, M. S. Hassanpour, H. Dehghani, A. Z. Snyder, T. Hershey, and J. P. Culver, "Mapping distributed brain function and networks with diffuse optical tomography," Nat. Photonics **8**(6), 448–454 (2014).
11. Y. Lin, M. T. Ghijsen, H. Gao, N. Liu, O. Nalcioglu, and G. Gulsen, "A photo-multiplier tube-based hybrid MRI and frequency domain fluorescence tomography system for small animal imaging," Phys. Med. Biol. **56**(15), 4731–4747 (2011).
12. F. Nouizi, M. Torregrossa, R. Chabrier, and P. Poulet, "Improvement of absorption and scattering discrimination by selection of sensitive points on temporal profile in diffuse optical tomography," Opt. Express **19**(13), 12843–12854 (2011).
13. A. Farina, M. Betcke, L. Di Sieno, A. Bassi, N. Ducros, A. Pifferi, G. Valentini, S. Arridge, and C. D'Andrea, "Multiple-view diffuse optical tomography system based on time-domain compressive measurements," Opt. Lett. **42**(14), 2822–2825 (2017).
14. M. Alayed, M. A. Naser, I. Aden-Ali, and M. J. Deen, "Time-resolved diffuse optical tomography system using an accelerated inverse problem solver," Opt. Express **26**(2), 963–979 (2018).
15. J. Wang, S. C. Davis, S. Srinivasan, S. Jiang, B. W. Pogue, and K. D. Paulsen, "Spectral tomography with diffuse near-infrared light: inclusion of broadband frequency domain spectral data," J. Biomed. Opt. **13**(4), 041305 (2008).
16. J. Ruiz, F. Nouizi, J. Cho, J. Zheng, Y. Li, J.-H. Chen, M.-Y. Su, and G. Gulsen, "Breast density quantification using structured-light-based diffuse optical tomography simulations," Appl. Opt. **56**(25), 7146–7157 (2017).
17. H. Vavadi, A. Mostafa, F. Zhou, K. S. Uddin, M. Althobaiti, C. Xu, R. Bansal, F. Ademuyiwa, S. Poplack, and Q. Zhu, "Compact ultrasound-guided diffuse optical tomography system for breast cancer imaging," J. Biomed. Opt. **24**(02), 1 (2018).
18. P. G. Anderson, J. M. Kainerstorfer, A. Sassaroli, N. Krishnamurthy, M. J. Homer, R. A. Graham, and S. Fantini, "Broadband optical mammography: chromophore concentration and hemoglobin saturation contrast in breast cancer," PLoS One **10**, e0117322 (2015).
19. A. Leproux, Y. M. Kim, J. W. Min, C. E. McLaren, W.-P. Chen, T. D. O'Sullivan, S.-H. Lee, P.-S. Chung, and B. J. Tromberg, "Differential diagnosis of breast masses in South Korean premenopausal women using diffuse optical spectroscopic imaging," J. Biomed. Opt. **21**(7), 074001 (2016).
20. Y. Yamada and S. Okawa, "Diffuse optical tomography: Present status and its future," Opt. Rev. **21**(3), 185–205 (2014).
21. L. Zhang, Y. Zhao, S. Jiang, B. W. Pogue, and K. D. Paulsen, "Direct regularization from co-registered anatomical images for MRI-guided near-infrared spectral tomographic image reconstruction," Biomed. Opt. Express **6**(9), 3618–3630 (2015).
22. M. Althobaiti, H. Vavadi, and Q. Zhu, "Diffuse optical tomography reconstruction method using ultrasound images as prior for regularization matrix," J. Biomed. Opt. **22**(2), 026002 (2017).
23. T. C. Kwong, M. Hsing, Y. Lin, D. Thayer, M. B. Unlu, M.-Y. Su, and G. Gulsen, "Differentiation of tumor vasculature heterogeneity levels in small animals based on total hemoglobin concentration using magnetic resonance-guided diffuse optical tomography in vivo," Appl. Opt. **55**(21), 5479–5487 (2016).
24. H. Dehghani, S. Srinivasan, B. W. Pogue, and A. Gibson, "Numerical modelling and image reconstruction in diffuse optical tomography," Philos. Trans. R. Soc., A **367**(1900), 3073–3093 (2009).

Biomedical Optics EXPRESS

25. V. Ntziachristos, A. G. Yodh, M. Schnall, and B. Chance, "Concurrent MRI and diffuse optical tomography of breast after indocyanine green enhancement," Proc. Natl. Acad. Sci. U. S. A. **97**(6), 2767–2772 (2000).
26. V. Rieke and K. Butts Pauly, "MR thermometry," J. Magn. Reson. Imaging **27**(2), 376–390 (2008).
27. F. Nouizi, A. Luk, D. Thayer, Y. Lin, S. Ha, and G. Gulsen, "Experimental validation of a high-resolution diffuse optical imaging modality: photomagnetic imaging," J. Biomed. Opt. **21**(1), 016009 (2016).
28. D. A. Thayer, Y. Lin, A. Luk, and G. Gulsen, "Laser-induced photo-thermal magnetic imaging," Appl. Phys. Lett. **101**(8), 083703 (2012).
29. A. Luk, F. Nouizi, H. Erkol, M. B. Unlu, and G. Gulsen, "Ex vivo validation of photo-magnetic imaging," Opt. Lett. **42**(20), 4171–4174 (2017).
30. Y. Lin, H. Gao, D. Thayer, A. L. Luk, and G. Gulsen, "Photo-magnetic imaging: resolving optical contrast at MRI resolution," Phys. Med. Biol. **58**(11), 3551–3562 (2013).
31. F. Nouizi, H. Erkol, A. Luk, M. Marks, M. B. Unlu, and G. Gulsen, "An accelerated photo-magnetic imaging reconstruction algorithm based on an analytical forward solution and a fast Jacobian assembly method," Phys. Med. Biol. **61**(20), 7448–7465 (2016).
32. H. Erkol, F. Nouizi, A. Luk, M. B. Unlu, and G. Gulsen, "Comprehensive analytical model for CW laser induced heat in turbid media," Opt. Express **23**(24), 31069–31084 (2015).
33. F. Nouizi, H. Erkol, A. Luk, M. B. Unlu, and G. Gulsen, "Real-time photo-magnetic imaging," Biomed. Opt. Express **7**(10), 3899–3904 (2016).
34. A. T. Luk, F. Nouizi, M. Marks, T. Kart, and G. Gulsen, "Monitoring gold nanoparticle distribution with high resolution using photo-magnetic imaging," Proc. SPIE **9706**, 97060M (2016).
35. M. Algarawi, F. Nouizi, A. Luk, H. Erkol, M. Almudhry, B. M. Unlu, S. Ha, and G. Gulsen, "Experimental validation of a multiple wavelength Photo-Magnetic Imaging system," in *Optical Tomography and Spectroscopy*, (Optical Society of America, 2020), STh3D. 3.
36. S. Arridge, "Optical tomography in medical imaging," Inverse Probl. **15**(2), R41–R93 (1999).
37. Q. Zhu, P. U. Hegde, A. Ricci Jr, M. Kane, E. B. Cronin, Y. Ardeshirpour, C. Xu, A. Aguirre, S. H. Kurtzman, and P. J. Deckers, "Early-stage invasive breast cancers: potential role of optical tomography with US localization in assisting diagnosis," Radiology **256**(2), 367–378 (2010).
38. Y. Lin, D. Thayer, O. Nalcioglu, and G. Gulsen, "Tumor characterization in small animals using magnetic resonance-guided dynamic contrast enhanced diffuse optical tomography," J. Biomed. Opt. **16**(10), 106015 (2011).
39. Y. Lin, W. C. Barber, J. S. Iwanczyk, N. E. Hartsough, W. Roeck, O. Nalcioglu, and G. Gulsen, "Quantitative fluorescence tomography using a combined tri-modality FT/DOT/XCT system," Opt. Express **18**(8), 7835–7850 (2010).
40. F. Nouizi, T. C. Kwong, J. Cho, Y. Lin, U. Sampathkumaran, and G. Gulsen, "Implementation of a new scanning method for high-resolution fluorescence tomography using thermo-sensitive fluorescent agents," Opt. Lett. **40**(21), 4991–4994 (2015).
41. A. Ale, R. B. Schulz, A. Sarantopoulos, and V. Ntziachristos, "Imaging performance of a hybrid x-ray computed tomography-fluorescence molecular tomography system using priors," Med. Phys. **37**(5), 1976–1986 (2010).
42. A. T. Luk, S. Ha, F. Nouizi, D. Thayer, Y. Lin, and G. Gulsen, "A true multi-modality approach for high resolution optical imaging: photo-magnetic imaging," in *SPIE BiOS*, (International Society for Optics and Photonics, 2014), 89370G–89377.
43. J. Y. Lee, J. T. Pierce, R. Zeh, S. S. Cho, R. Salinas, S. Nie, and S. Singhal, "Intraoperative near-infrared optical contrast can localize brain metastases," World Neurosurg. **106**, 120–130 (2017).
44. Z.-Z. J. Lim, J.-E. J. Li, C.-T. Ng, L.-Y. L. Yung, and B.-H. Bay, "Gold nanoparticles in cancer therapy," Acta Pharmacol. Sin. **32**(8), 983–990 (2011).
45. P. Taroni, A. M. Paganoni, F. Ieva, A. Pifferi, G. Quarto, F. Abbate, E. Cassano, and R. Cubeddu, "Non-invasive optical estimate of tissue composition to differentiate malignant from benign breast lesions: A pilot study," Sci. Rep. **7**(1), 40683–11 (2017).